

Musah, J.-D., Ilyas, A.M., Novitskii, A., Serhiienko, I., Egbo, K. O., Saianand, G., Khovaylo, V., Kwofie, S., Yu, K. M. and Roy, V. A.L. (2021) Effective decoupling of seebeck coefficient and the electrical conductivity through isovalent substitution of erbium in bismuth selenide thermoelectric material. *Journal of Alloys and Compounds*, 857, 157599. (doi: [10.1016/j.jallcom.2020.157559](https://doi.org/10.1016/j.jallcom.2020.157559))

There may be differences between this version and the published version. You are advised to consult the publisher's version if you wish to cite from it.

<http://eprints.gla.ac.uk/224232/>

Deposited on 21 October 2020

**Effective Decoupling of Seebeck Coefficient and the Electrical Conductivity
through Isovalent Substitution of Erbium in Bismuth Selenide
Thermoelectric Material**

Jamal-Deen Musah¹, A.M Ilyas¹, Andrei Novitskii², Illia Serhiienko², Kingsley O. Egbo³, Gopalan Saianand⁴, Vladimir Khovaylo^{2,5,6}, Samuel Kwofie⁷, Kin Man Yu³, Vellaisamy A.L. Roy^{8}*

¹Department of Material Science and Engineering and State Key Laboratory of Terahertz and Millimeter Waves, City University of Hong Kong, Kowloon Tong, Hong Kong, S.A.R.

²National University of Science and Technology "MISiS", Moscow 119049, Russia

³Department of Physics, City University of Hong Kong, Kowloon Tong, Hong Kong, S.A.R.

⁴Global Centre for Environmental Remediation (GCER), Faculty of Science, The University of Newcastle, Callaghan 2308, New South Wales, Australia

⁵National Research South Ural State University, Chelyabinsk 454080, Russia

⁶Chelyabinsk State University, Chelyabinsk 454001, Russia

⁷Department of Materials Engineering, Kwame Nkrumah University of Science and Technology (KNUST), Kumasi – Ghana

⁸James Watt School of Engineering University of Glasgow, G128QQ, United Kingdom

**Corresponding author: Roy.Vellaisamy@glasgow.ac.uk*

Abstract

Recognizing high thermoelectric performance in semiconducting materials is a challenging task. This is because the Seebeck coefficient and electrical conductivity which constitute the thermoelectric power factor are unfavourably coupled. This means decoupling the transport properties of thermoelectric materials to enhance the power factor without compromising the thermal conductivity is essential. Herein we report that the substitution of erbium (Er) within bismuth selenide (Bi_2Se_3) results in a simultaneous enhancement in Seebeck coefficient and electrical conductivity *via* effective mass and Fermi energy optimization. The Er-Substitution in Bi_2Se_3 does not only promote a simultaneous increase in Seebeck coefficient and electrical conductivity but also decreases the thermal conductivity through an enhancement in phonon scattering.

Consequently, the optimum composition is found for the $\text{Bi}_{1.85}\text{Er}_{0.15}\text{Se}_3$ sample instigating that, minimal substitution amount is required to optimize the thermoelectric performance. Our numerical calculation also shows that Er substitution alters the Fermi energy of the Bi_2Se_3 TE materials, thereby enhancing the effective mass. Through Raman and XPS characterization, we also elucidate that Er substitution does not change the chemical structure and chemical bonding of the pristine material appreciably. It thus leads to improvement in the Seebeck coefficient and electrical conductivity via effective mass optimization. This unique work presents a facile, scalable, cost-effective, and controllable synthesis of nanostructured Bi_2Se_3 toward realizing high-performance thermoelectric devices.

KEYWORDS: Thermoelectric material; Isovalent Substitution; Bismuth selenide; Power Factor

1. Introduction

Thermoelectric (TE) devices are of paramount importance in the clean energy sector owing to their beneficial traits such as light-weight, scalable, and can be integrated into devices (micro/nano) for power generation (heating/cooling applications). The direct conversion of low-grade heat energy into useful electrical energy via the TE effect is remarkable. This is because, not only does it provide a green solution to sustainable energy demand, it also offers optimum utilization of waste energy^{1,2}. The efficiency of TE material performance (zT) is linearly dependent on the product of Seebeck coefficient (S) and electrical conductivity (σ), $S^2\sigma$, and inversely proportional to the total thermal conductivity κ_T . A strategy to concomitantly enhance the Seebeck coefficient and the electrical conductivity is essential as this will improve the power factor ($S^2\sigma$) and hence ensure optimum TE performance. The dilemma is the intrinsic coupling of S and σ such that an increase in one promotes a decrease in the other. This has made it extremely difficult to enhance the power factor (PF) substantially. To ensure efficient improvement in the TE performance, the Seebeck coefficient and the electrical conductivity need to be decoupled for bulk-inorganic material such as Bi_2Te_3 , Bi_2Se_3 , Sb_2Te_3 , etc. Seebeck coefficient value is estimated by the asymmetry in the density of state (DOS) considered above and below the Fermi level. Similarly, the electrical conductivity is calculated by the product of carrier concentration and carrier mobility. However, a significantly high Seebeck coefficient demands a large asymmetry in the DOS across the Fermi level. This is contrary to the enhancement direction of the carrier concentration. This makes it problematic to achieve a simultaneous enhancement in both S and σ . For that reason, several researchers focus attention on reducing the lattice thermal conductivity via phonon/defect engineering.³ This attempt has seen success to a smaller extent in effectively improving the zT because the thermal conductivity has been proven to be restrained by the amorphous limit.⁴ Therefore, simultaneously improving S and σ is highly desirable for realizing high TE performance.

Isovalent substitution has been considered as a prominent strategy to decouple the electrical conductivity and Seebeck coefficient. Towards this end, Devender *et al.*⁵ experimentally and

theoretically studied the influence of anionic site substitution of selenium with sulphur in $\text{Bi}_2\text{Te}_2\text{Se}$ (n-type) thermoelectric material. It was revealed that a small substitution amount of Se for S causes profound changes to the energy band structure. This leads to an improvement in the effective mass (m^*) and thus results in simultaneous enhancement of the σ and S. In the same way, Vaney et al.,⁶ investigated the effect of tellurium substitution with selenium on the electronic band structure and the TE properties of $\text{As}_2\text{Te}_{3-x}\text{Se}_x$. The studies revealed that the lower substitution amount did not significantly alter the density of state as well as the energy band gap at the Fermi level. However, with an increase in Se substitution, there was an increased electrical conductivity and thermopower coupled with reduced thermal conductivity. This contributed to enhancement in the TE performance.

Similarly, in our recent study, Musah *et al.*⁷ adopted an isovalent substitution of Bi with cerium (Ce) in Bi_2Se_3 TE material. This substitution strategy essentially controls the carrier density by accessing fine features of the energy band structure of thermoelectric materials and hence promoting the simultaneous enhancement of the thermopower and the electrical conductivity. The results showed a simultaneous improvement of the electrical conductivity and the Seebeck coefficient. Considering the difference in the atomic size of Ce and Er, we have studied the impact of a large rare earth element (Erbium, Er) substitution in Bi_2Se_3 thermoelectric material. Herein, we present substitution of Er in Bi_2Se_3 as evidence of rare earth metal influence on decoupling the Seebeck coefficient and the electrical conductivity, which leads to simultaneous enhancement in the performance of Bi_2Se_3 TE material. To the best of the author's knowledge, a detailed investigation of Er substitution into Bi_2Se_3 toward improving thermoelectric power factor by carefully considering various beneficial associated material properties has not been studied. Besides, we judiciously tune the proportions of Er and systematically investigated the structural, morphology, and electronic properties of a range of as-developed Bi_2Se_3 bulk samples and characterized them through appropriate techniques.

2. Experimental Section

2.1. Synthesis Procedure of the Bulk $\text{Bi}_{2-x}\text{Er}_x\text{Se}_3$ ($x = 0, 0.15, 0.3, 0.4$) Powder

$\text{Bi}_{2-x}\text{Er}_x\text{Se}_3$ ($x = 0, 0.15, 0.3, 0.4$) powder were prepared through a facile one-pot solvothermal method. Typically, bismuth (Bi) nitrate pentahydrate ($\text{Bi}(\text{NO}_3)_3 \cdot 5\text{H}_2\text{O}$, (98% J&K Scientific Ltd.), Erbium nitrate hexahydrate ($\text{Er}(\text{NO}_3)_3 \cdot 6\text{H}_2\text{O}$, Aldrich, 99.99%), Selenium powder (99% Se powder, J&K Scientific Ltd.), 2-methoxy ethanol anhydrous (99.8% Sigma Aldrich), and ethanolamine ($\geq 99.0\%$ ACS reagent, Aldrich) were used. The required volume ratio of 2-methoxy ethanol and ethanolamine were mixed with the measured quantity of $\text{Bi}(\text{NO}_3)_3 \cdot 5\text{H}_2\text{O}$, $\text{Er}(\text{NO}_3)_3 \cdot 6\text{H}_2\text{O}$, and Se powder. Then, the above mixture is kept in a Teflon lined autoclave reactor and maintained at 463K for 24 hrs. Finally, the various Er-doped compositions of Bi_2Se_3 are obtained *via* centrifugation with distilled water and then dried at 343K. The schematic synthesis procedure is shown in **Figure 1**.

2.2. Characterization of $\text{Bi}_{2-x}\text{Er}_x\text{Se}_3$ Samples

The synthesized $\text{Bi}_{2-x}\text{Er}_x\text{Se}_3$ bulk samples were characterized by X-ray diffraction (XRD Bruker SRD –D2 Phaser with a slit size of 1mm) using Cu K α radiation. We used a scan step size of 0.02° with 0.1 seconds per step. Similarly, the morphology of the as-synthesized samples was analyzed by scanning electron microscopy (FEI Quanta 450). The results of the elemental composition are shown in **Figure S-1** and **Table S-1** in the **Supporting Information (SI)**. The Raman equipment (Renishaw 2000 microscope) equipped with a HeNe laser (632.8nm) and Scanning Auger - X-ray Photoemission Spectroscopy (XPS), (PHI model 5802) were used to characterize the samples. The obtained $\text{Bi}_{2-x}\text{Er}_x\text{Se}_3$ powder was made into disc-shaped samples with a thickness of 0.7 mm and a diameter of 13 mm with a pressure of 20 MPa using a cold-press method. The obtained raw pellets were subjected to vacuum annealing at 593K for a day. The heat treatment temperature is selected based on the optimization studies already reported for pristine Bi_2Se_3 bulk material.⁷ Using Archimedes' principle approach, the densities of the all the samples were determined to be 97%, 95%, 92% and 96% for Bi_2Se_3 , $\text{Bi}_{1.85}\text{Er}_{0.15}\text{Se}_3$, $\text{Bi}_{1.7}\text{Er}_{0.3}\text{Se}_3$, and $\text{Bi}_{1.6}\text{Er}_{0.4}\text{Se}_3$ respectively compared to the theoretical density (6.79 gcm^{-3}).⁸

2.3. Evaluation of Thermoelectric Properties

The Seebeck coefficient (S), electrical conductivity (σ_{ZEM}) were measured at temperatures from 300 K to 473 K using a Seebeck coefficient/electrical resistance measuring system (CRYOTEL). All the $\text{Bi}_{2-x}\text{Er}_x\text{Se}_3$ pellets for S and σ measurements were cut into a rectangular bar-shaped (12.7 mm \times 7 mm \times 0.5 mm) samples. The thermal diffusivity (D) and specific heat capacity (Cp) measurement were carried out by laser flash method (LFA 457; Netzsch) and differential scanning calorimetry (DSC 404F; Netzsch) respectively. The Archimedes procedure was then used to determine the density (ρ). We, therefore, calculated the thermal conductivity (K_T) using $k_T = \rho \times D \times C_p$. Besides, the Hall-effect system (ECOPIA HMS-5300) is used to measure the Hall coefficient (300K) in the Van der Pauw configuration using the current and magnetic fields of 2 mA and 0.5 T respectively. Here, the electron mobility (μ_H) and electron density (n_H) are estimated using the relation $\mu_H = \sigma R_H$ and $n_H = \frac{1}{eR_H}$.

3. Results and Discussion

The XRD patterns of all the $\text{Bi}_{2-x}\text{Er}_x\text{Se}_3$ ($x = 0, 0.15, 0.3$ and 0.4) samples are shown in **Figure 2a**. All the diffraction peaks of the synthesized samples are well indexed to the Bi_2Se_3 hexagonal phase (JCDPS card No. 33-0214). This suggests the formation of a single-phase for the Bi_2Se_3 based samples without secondary phases within the detectability limits of the X-ray diffraction. The slight shift of the XRD spectra to a higher 2θ show that Er incorporation in the Bi_2Se_3 structure leads to shrinkage of the crystal structure. The lattice parameters a and c were calculated using the procedure shown in Ref. ⁹, and the results are presented in **Table 1**. Upon increase in Er substitution ($0 < x < 0.4$), the lattice parameter, as well as the lattice volume, decreases slightly with Er content which is consistent with the small difference in the ionic/covalent radius of Er^{3+} (1.00 Å /1.57 Å) compared with Bi^{3+} (1.03 Å /1.46 Å). However, as the Er amount reached $x = 0.4$, the crystal structure showed lattice expansion. This implies that with increasing Er content, more Er^{3+} ions substitute Bi^{3+} in the unit cell of the $\text{Bi}_{2-x}\text{Er}_x\text{Se}_3$, which then leads to crystal lattice variation. Also, Er_2Se_3 structure (orthorhombic) has a lattice parameter ($a, b,$ and c) of 8.085, 11.346, and 24.14 Å, respectively ¹⁰

compared to the hexagonal structure of the Bi_2Se_3 ($a = 4.134 \text{ \AA}$ and $c = 28.576 \text{ \AA}$). The larger lattice parameter (a and b) of Er_2Se_3 compared to that of Bi_2Se_3 ($a = b = 4.134 \text{ \AA}$) is responsible for the variation in the lattice parameter of the Er substituted samples. Thus, the variations in the lattice parameter and volume in the unit cell with increasing Er content are expected. Similar behaviour is observed in our earlier work ⁷ for cerium substitution for Bi in Bi_2Se_3 TE material. For semiconductors, the lattice parameters depend on the concentration of dopants, defects, strain, and ionic radii difference with respect to the host ¹¹. To investigate the possibility of the formation of crystallographic texture, we have compared the XRD results of both the synthesized powder and the pellet in **Figure S-2**. Similarly, the variation in the peak position and intensity of both the powder and the pellets are compared in **Figure S-3a** and **Figure S-3b**, respectively. The unnoticeable difference in the XRD for both the powder and the pellet imply the absence of crystallographic texture in the final pellet. We adopted the Scherrer's relation¹² to estimate the average crystallite size, D_{hkl} (**Eqn 1**) for all the $\text{Bi}_{2-x}\text{Er}_x\text{Se}_3$ ($x = 0, 0.15, 0.3, 0.4$) samples.

$$D_{hkl} = \frac{k\lambda}{\beta_{hkl} \cos\theta} \quad (1)$$

Where λ , β , and θ , (hkl) and k is the wavelength of the X-ray used (1.5406 \AA), the full width at half maximum in radian along (015) plane, Bragg's diffraction angle, the Miller indices of the (015) plane and k is the Scherrer constant.

Table 1. The summary of obtained peak positions, d -spacing, cell parameter, and lattice volume variations of the as-prepared $\text{Bi}_{2-x}\text{Er}_x\text{Se}_3$ ($x = 0, 0.15, 0.3, 0.4$) samples.

Sample designation	Peak position 2θ ($^\circ$)	d-spacing (\AA)	Cell parameters(\AA)		Volume (\AA^3)	FWHM, β ($^\circ$)
			a = b	c		
Bi_2Se_3	43.757	2.067	4.134	28.576	422.988	0.1487
$\text{Bi}_{1.85}\text{Er}_{0.15}\text{Se}_3$	43.8064	2.065	4.129	28.481	420.674	0.1654
$\text{Bi}_{1.7}\text{Er}_{0.3}\text{Se}_3$	43.882	2.062	4.123	28.346	417.304	0.2014
$\text{Bi}_{1.6}\text{Er}_{0.4}\text{Se}_3$	43.759	2.067	4.134	28.549	422.539	0.1903

The FWHM (β) of all the samples considered for the highly intense peak (015) is shown in **Table 1**. The β of all the Er substituted samples are higher than that of the undoped pristine sample (Bi_2Se_3) indicating the reduced crystallite size of the $\text{Bi}_{2-x}\text{Er}_x\text{Se}_3$ ($x>0$) samples. Similarly, the increase in β with Er-substitution (for $x < 0.4$) shows crystal lattice distortion and crystallinity deterioration ¹³.

Figure 2b shows the peak position and intensity variation for all the samples. As can be seen, there is no significant variation in the peak intensities for samples, $x < 0.4$. However, for the highly substituted sample ($x = 0.4$), the peak position does not only show the lowest intensity but also shifts to a lower angle 2θ . The reduced peak intensity and the FWHM increase with doping are due to the degradation of crystallinity in all the Er-doped samples ¹⁴, which manifested in the electrical conductivity measurement (**Figure 6a**). From **Eqn S-1**, the degree of the crystallinity has been estimated, and the result is shown in **Figure S-3c**. It could be realized that, with the introduction of the Er as a dopant, the crystallite size (**Figure 2c**) and the degree of crystallinity decreases. The decrease in the crystallinity is responsible for the deterioration of the mobility and electrical conductivity for the highly doped samples.

Figure S-4 is the FEG-SEM morphology of all the synthesized powder samples. Plates-like morphology of varying sizes are observed for all the samples where the average crystallite size was estimated to decrease with Er-substitution. The reduced crystallite size for the Er containing samples reflected in the thermal conductivity reduction. This is so because the smaller crystallite sizes increase the number of crystal boundaries, which eventually enhances grain boundary induced phonon scattering and consequently reduced lattice thermal conductivity. **Table S-2** compares crystallites sizes obtained via (**Eqn 1**) and SEM. The crystallite size decrease from 55 nm ($x = 0$) to 44 nm ($x = 0.4$) with a negligible difference in the crystallites size obtained with the two methods. Furthermore, the EDX analysis for the $\text{Bi}_{2-x}\text{Er}_x\text{Se}_3$ samples is shown in **Figure S-1**, and the corresponding EDX mapping is shown in **Figure S-5** (showing homogeneity of the final product). It is observed that the Er and Se peaks (EDX) overlap which can be ascribed to the inherent limitation

of the EDX technique as a consequence of the X-rays which are generated by the emission from several energy level shells (K, L, M)¹⁵.

The Raman spectroscopy was used to show the vibrational modes in the synthesized $\text{Bi}_{2-x}\text{Er}_x\text{Se}_3$ materials. The result is depicted in **Figure 3** showing two typical Raman active modes E_g^2 , and A_{1g}^2 obtained at wavenumbers of 134 cm^{-1} and 176 cm^{-1} respectively for the pristine sample (Bi_2Se_3). The peak found at 256 cm^{-1} is linked to the interchain bond strength vibrational mode of the disordered Se chains¹⁶. Here, the "A" and "E" denote the out-of-plane and in-plane lattice vibration (**Figure 3b**) respectively, and the subscript "g" represents the Raman active mode. It is also evident that, after the introduction of the dopant (Er) in various quantities ($0 \leq x \leq 0.4$), there is no change in the peak position for all the peaks. This is so because the substitution of the impurity atom (with similar atomic radius to the host) offered no significant alteration in the chemical structure and bond length.¹⁷ Although four Raman active peaks ($2A_{1g} + 2 E_g$) are evident for Bi_2Se_3 materials,¹⁸ several studies, however, have only shown the existence of one to three peaks^{19–22}. These discrepancies are probably due to the inaccessibility to probing due to the filtration of the either high or low-frequency shift in the Raman set-up. The individual Raman tensors defining the Raman active peaks are related as

$$E_g \rightarrow \begin{pmatrix} c & 0 & 0 \\ 0 & -c & d \\ 0 & d & 0 \end{pmatrix} \text{ or } \begin{pmatrix} 0 & -c & -d \\ -c & 0 & 0 \\ -d & 0 & 0 \end{pmatrix} \quad (2)$$

$$A_{1g} \rightarrow \begin{pmatrix} a & 0 & 0 \\ 0 & a & 0 \\ 0 & 0 & b \end{pmatrix} \quad (3)$$

It could be seen that the Raman tensor is distinguished by the off-diagonal of the individual vibrational modes (**Eqn 2 and 3**)²³. The Raman spectra were recorded at room temperature using a Renishaw 2000 microscope equipped with a HeNe laser (632.8nm) with a laser power of 15 mW and an integration time of 20 ms focused on the sample. The selected power was to prevent the laser heating effect on the samples.

The XPS technique is utilized to obtain the binding energies of the core-level of each of the atoms (Bi, Er, and Se) constituting the $\text{Bi}_{2-x}\text{Er}_x\text{Se}_3$ compound. **Figure 4** and **Table 2** represents the data obtained from the XPS studies. The XPS spectra show C1s peak at 248 eV. As can be seen, the high resolution spectral of Se, Er and Bi did not show any significant change in the binding energies of the pristine as well as the Er – substituted samples. This implies, the substitution of Bi^{3+} for Er^{3+} (of comparable atomic size) in the Bi_2Se_3 compound does not significantly alter the chemical bond and hence the chemical structure²⁴. The Bi $4f_{7/2}$ and Bi $4f_{5/2}$ peaks for the pristine are observed at binding energies of 157.05 eV, 158.06 eV, and 162.36 eV, 163.36 eV respectively. These values, however, varied slightly (~ 0.25 and 0.4 eV for both $4f_{7/2}$ and $4f_{5/2}$) for all the Er-substituted samples. Similarly, for the Se $3d_{5/2}$ (53.38 eV) and Se $3d_{3/2}$ (54.19 eV) peaks for the pristine remain unchanged for all the Er substituted samples. More importantly, the Er 4d for all the Er containing samples show binding energy of 177.64 eV ($x = 0.15$), 177.7 eV ($x = 0.3$ and 177.94 eV). The binding energies for the dopant (Er) can be assigned to Er^{+3} ,²⁵, confirming that, the Er^{3+} successfully substituted the Bi^{3+} . The area and FWHM obtained from the fitted peaks are shown in **Table S-3**. The area and the width of the Er-4d core-level spectra increase with doping content. The increase in FWHM and area of the Er-4d with doping suggest that the effect of the Er^{3+} ions in the Bi_2Se_3 lattice dominant as x is varied from 0.15 to 0.4. Also, the elemental composition has been estimated from the XPS characterization. The XPS data is compared with the EDX in **Table S-1**. Similar composition for the $\text{Bi}_{2-x}\text{Er}_x\text{Se}_3$ is found for the two techniques with both methods showing the presence of small Se vacancies which add to the n of the synthesized samples.

Table 2 The individual XPS data obtained for the $\text{Bi}_{2-x}\text{Er}_x\text{Se}_3$ materials.

Sample designation	Core-level Binding Energy (eV)						
	Bi				Se		Er
	$4f_{7/2}$		$4f_{5/2}$		$3d_{5/2}$	$3d_{3/2}$	3d
Bi_2Se_3	157.05	158.06	162.36	163.36	53.38	54.19	--
$\text{Bi}_{1.85}\text{Er}_{0.15}\text{Se}_3$	156.80	157.68	162.11	162.96	53.27	54.10	177.70
$\text{Bi}_{1.7}\text{Er}_{0.3}\text{Se}_3$	156.80	157.68	162.11	162.96	53.25	54.09	177.60
$\text{Bi}_{1.6}\text{Er}_{0.4}\text{Se}_3$	156.80	157.69	162.09	162.96	53.25	54.08	177.60

To investigate the effect of isovalent substitution on the electronic transport properties of Bi₂Se₃, the Hall electron mobility, electron concentration, Seebeck coefficient, electrical and thermal conductivity were measured and shown in **Figure (5) and (6)**. The optimal Er concentration leading to the highest TE performance is $x = 0.15$. The room temperature Hall measurement of all our samples are presented in **Table 3**. The electron concentration increases from $x = 0$ to $x = 0.15$ and then decrease until $x = 0.4$. Similarly, the Hall mobility of the Er containing samples is lower than that of the pristine. It is understood that the isovalent substitution controls the electron concentration and improves electron mobility of metal chalcogenides ^{7,26}. However, the low mobility in the Er-substituted samples compared to the undoped could be attributed to the creation of the lattice distortion caused by the dopant (due to the slight difference in the atomic radius of the dopant (Er) and the host (Bi) atom) ²⁷.

Similarly, compared to our previous studies on cerium substitution in Bi₂Se₃, the rate of deterioration of electron mobility in the present study is faster due to the larger atomic size of Er compared with Ce. Hume Rothery (H-R) has explained that an atomic mismatch in a solid solution influences lattice distortion. From H – R theory, the atomic mismatch is defined as in **Eqn 4**

$$\text{Atomic mismatch} = \left[\frac{|r_i - r_j|}{r_j} \right] \leq 15\% \quad (4)$$

Where r_i and r_j are the atomic radius of the solute (Er) and the solvent (Bi) atoms, respectively. From **Eqn 4**, it is estimated that the atomic factor exceeding 15% leads to solid solution mismatch ²⁸. The atomic mismatch found for Bi_{2-x}Er_xSe₃ is 50%. This distortion of the lattice by Er substitution could have resulted in reduced electron mobility. It is worth noting that, besides the possible atomic mismatch as well as scattering effect on electron mobility, chemical bond type (ionic or covalent) also significantly influences the electron mobility of a material. ²⁹ Ionic bonds are less favourable for the transport of carriers (higher ionic component decreases the mobility of charges) compared to covalent bonds ³⁰. The ionic part of any A-B type bond is estimated by the Pauli empirical formula (**Eqn 5**).

$$\text{Bond (ionic component)} = 1 - \text{Exp} \left[\frac{-(X_A - X_B)^2}{4} \right] \quad (5)$$

Where X_A and X_B are the respective electronegativities. Hence considering the electronegativities of Er (1.24) and Bi (2.02), the calculated ionic component of Er-Se (**34.9%**) is much higher than that of Bi-Se (**6.8%**) and hence exhibit lower electron mobility than that of pure Bi-Se. The low electron mobility of the Er-doped samples could also be due to the higher degree of ionic bond in the Er-Se ($\text{Bi}_{2-x}\text{Er}_x\text{Se}_3$) compared to Bi-Se (Bi_2Se_3) samples.

Rare earth elements are regarded as intermetallic compounds, and their 4f energy levels are positioned near the Fermi energy level and hence form a narrow-parabolic band leading to an improved density of state and Seebeck values³¹. It is therefore not surprising that the m^* of the $\text{Bi}_{2-x}\text{Er}_x\text{Se}_3$ samples increased from $x = 0$ to $x = 0.15$ and then decrease with further increase in Er substitution. The improvement in the m^* leads to enhancement in the Seebeck coefficient.

Table 3. Room temperature thermoelectric properties of $\text{Bi}_{2-x}\text{Er}_x\text{Se}_3$ ($x = 0, 0.15, 0.3, 0.4$) material.

Sample	n_{Hall} (10^{18}cm^{-3})	μ_{Hall} ($\text{cm}^2\text{V}^{-1}\text{s}^{-1}$)	σ_{Hall} (Scm^{-1})	σ_{ZEM} (Scm^{-1})	S (μVK^{-1})	κ_T ($\text{Wm}^{-1}\text{K}^{-1}$)
Bi_2Se_3	1.86	149	44.34	36.39	-109.97	0.83
$\text{Bi}_{1.85}\text{Er}_{0.15}\text{Se}_3$	3.03	51.06	24.72	34.54	-114.23	0.54
$\text{Bi}_{1.7}\text{Er}_{0.3}\text{Se}_3$	1.60	28.17	7.19	8.68	-112.23	0.36
$\text{Bi}_{1.6}\text{Er}_{0.4}\text{Se}_3$	1.23	42.15	8.29	10.61	-114.01	0.29

Considering the transport equation within the approximation that, the mean free path is independent of charge carrier energy, the Seebeck coefficient is given by the as; **(Eqn 6)**³²:

$$S = \left(\frac{2}{3} \right) \frac{C_v}{ne} \quad (6)$$

Where C_v is the volume-specific heat, n is the electron concentration, and e is the electrical charge. However, when the relaxation time is regarded as constant (when the energy dependence of free mean path is constant), Eqn (6) reduces to Eqn (7)³³

$$S = -\left(\frac{1}{3}\right) \frac{\pi^2 K_B^2}{e E_F} T \quad (7)$$

From **Eqn 7** and using the measured Seebeck coefficient, the Fermi energy, E_F concerning the conduction band ($E_F - E_C$) of thermoelectric materials are determined. In this case, the effect of Er doping on the Fermi energy is shown in **Figure 5c**. From this data, it is evident that the Fermi energy responds to the inclusion of the isovalent dopant in the Bi_2Se_3 crystal structure. At 300K, the Fermi energy decreases from 67 meV (Bi_2Se_3) to 64 meV ($\text{Bi}_{1.85}\text{Er}_{0.15}\text{Se}_3$). This value remains nearly the same for $\text{Bi}_{1.7}\text{Er}_{0.3}\text{Se}_3$ (65 meV) and $\text{Bi}_{1.6}\text{Er}_{0.4}\text{Se}_3$ (64 meV). This slight shift of the Fermi energy towards the valence band coupled with the broadening of the valence band as shown in our previous study ⁷ is essential for supporting simultaneous enhancement in the Seebeck coefficient ³² and electrical conductivity.

Figure 6 shows the temperature dependence of the thermoelectric transport properties of the pristine (Bi_2Se_3) and Er-doped samples measured perpendicular to the direction of applied pressure during pelleting. In **Figure 6a**, the temperature dependence of the electrical conductivity of the $\text{Bi}_{2-x}\text{Er}_x\text{Se}_3$ samples is shown. We observe that the $\text{Bi}_{2-x}\text{Er}_x\text{Se}_3$ show a monotonic increase in both the electrical conductivity (**Figure 6a**) and the Seebeck coefficient (**Figure 6b**) throughout the entire temperature range. The effect of Er substitution in Bi_2Se_3 sample is obviously seen from $x = 0$, to $x = 0.4$. The room temperature electrical conductivity of the pristine sample ($x = 0$) is 36 Scm^{-1} . This value increases monotonically to 40 Scm^{-1} at 473K. With the inclusion of the Er dopant ($x = 0.15$), σ slightly reduces to 34 Scm^{-1} at room temperature, which then increases to 50 Scm^{-1} at 473K. However, as the dopant amount was further increased to $x = 0.3$ and 0.4 , the electrical conductivity values dropped by 76% and 71% respectively, at 300K. Comparatively, $\text{Bi}_{1.85}\text{Er}_{0.15}\text{Se}_3$ sample shows the best performance in terms of electrical conductivity. This implies, less substitution of Er for Bi in Bi_2Se_3 is crucial for improving the electrical performance as also suggested by Devender *et al.* ⁵ in sulphur doped $\text{Bi}_2\text{Te}_2\text{Se}$ TE material. **Figure 6b** displays the Seebeck coefficient dependence on temperature for all the $\text{Bi}_{2-x}\text{Er}_x\text{Se}_3$ samples. The negative values of the Seebeck coefficient are

indicative of *n*-type semiconductor behaviour for all our samples. As shown in **Figure 6b**, the Seebeck coefficient gradually increases with increasing Er content with the maximum value obtained to be $150 \mu\text{VK}^{-1}$ for $\text{Bi}_{1.6}\text{Er}_{0.4}\text{Se}_3$ at 473K. The isovalent substitution of Er into Bi_2Se_3 is optimized for $x = 0.15$ for improved TE performance at 473K. The enhancement in the TE properties is attributed to the less contribution of neutral impurity scattering³⁴ to electronic transport properties. The power factor (PF) of $\text{Bi}_{2-x}\text{Er}_x\text{Se}_3$ samples has been determined using the experimental values of S and σ . **Figure 6c** shows the temperature dependence of the PF. It is clear from **Figure 6c** that the power factor is improved from the pristine to $x = 0.15$ sample, which then deteriorates significantly for the higher loadings of Er ($x = 0.3$ and 0.4). The enhancement of the PF is significant for the less substituted sample ($x = 0.15$) elucidating the effectiveness in the minimal dopant contribution to the thermoelectric properties. Since the PF doubly depends on the Seebeck coefficient ($S^2\sigma$), any little change in S will be manifested in the PF. In this regard, effectively, enhancing S and σ is one of the primary routes to improving TE performance.

The temperature-dependence of the total thermal conductivity of all the synthesized samples is shown in **Figure 6d** and similarly, the thermal diffusivity (**Figure S-6a**), specific heat (**Figure S-6b**) properties are shown. K_T of the pristine sample is $0.75 \text{ Wm}^{-1}\text{K}^{-1}$ at 300K and $0.62 \text{ Wm}^{-1}\text{K}^{-1}$ at 473K. For Er content of 0.15, K_T drastically reduces to $0.54 \text{ Wm}^{-1}\text{K}^{-1}$ (300K) and $0.41 \text{ Wm}^{-1}\text{K}^{-1}$ (473K). This reduction trend continuous until $x = 0.4$ ($K_T = 0.29 \text{ Wm}^{-1}\text{K}^{-1}$ at 473K). It must be noted that the total thermal conductivities of all the Er-doped samples remain lower than the pristine sample throughout the measured temperature range. This is due to the enhanced phonon scattering because of the Er-induced lattice distortion and reduced crystallite size. Defects and crystallite sizes are expected to improve short wave phonon scattering leading to a reduction in the lattice thermal conductivity and hence lower total thermal conductivity. Similarly, small grain sizes create interfaces for enhancing phonon grain boundary scattering³⁵⁻³⁷. This is seen in the low lattice thermal conductivity in the $\text{Bi}_{2-x}\text{Er}_x\text{Se}_3$ ($x > 0$) samples. The lattice thermal conductivity of the Er-doped samples is significantly decreased, which results in a significant reduction in the overall total thermal

conductivity of the $\text{Bi}_{2-x}\text{Er}_x\text{Se}_3$ ($x > 0$) samples. Also, the electronic thermal conductivity (κ_e) was determined using Weidman Franz law related by **Eqn 8**,

$$\kappa_e = L\sigma T = L(ne\mu)T \quad (8)$$

From **Eqn 8** n , L , e , μ , and T denote electron concentration Lorentz number, electronic charge, electron mobility, and temperature. The respective values of L is obtained from **Eqn S-2** . Using **Eqn 8**, the electronic thermal conductivity (**Figure S-6c**) was determined. Then, by using $k_l = K_T - K_e$, the lattice thermal conductivity is estimated. The calculated K_l is shown in **Figure S-6d**. The decrease in the K_l with Er substitution is due to the increase in the phonon scattering and possible interfacial scattering at grain boundaries. The sample with the best lattice thermal conductivity is the highly doped samples: $\text{Bi}_{1.7}\text{Er}_{0.3}\text{Se}_3$ ($0.349 \text{ Wm}^{-1}\cdot\text{K}^{-1}$ at 300K) and $\text{Bi}_{1.6}\text{Er}_{0.4}\text{Se}_3$ ($0.246 \text{ Wm}^{-1}\cdot\text{K}^{-1}$). Despite the ultralow thermal conductivity in the highly substituted samples, the TE performance is still poor due to the ultra-low electrical conductivity values. Disorder in TE materials enhances K_l reduction within the unit cell. This disorderliness is usually created via interstitials, rattling atoms, or occupancies coupled with the intrinsic disorder introduced by alloying. Phonon scattering is dependent on the mass ratio of the alloy constituents. This is seen in the k_T of the present work (Er-doped, Er/Bi) with a higher mass ratio compared with the previous study (Ce doped, Ce/Bi) ⁷. The TE measurements in this study and the previous work ⁷ indicate that a simultaneous enhancement of σ and S arise from a subtle variation in the electronic band structure leading to an increase in effective mass m^* . Minimal doping is essential for profound changes in the transport properties of topological insulators ⁵. This is due to the sensitivity of topological insulator band structure features.

We, therefore, demonstrate that Er induces simultaneous enhancement in Seebeck coefficient and electrical conductivity which is expected to influence the inverted conduction band of $\text{Bi}_{2-x}\text{Er}_x\text{Se}_3$ topological insulators. The recent work of Shi et al. ³⁸ suggested a possibility of simultaneous enhancement in S and σ for chalcogenides due to the band inversion features and Fermi surface anisotropy in topological insulators. Similarly, it has also been shown experimentally by our recent

work ⁷ and this current study that, rare earth substitution for Bi in Bi₂Se₃ is crucial for establishing simultaneous enhancement in TE properties and hence lead to an improvement in the zT.

The figure of merit defining the TE performance is calculated for all our samples by using the results obtained for electronic and thermal transport properties. The data of which is shown in **Figure 7**. The zT first increases with Er substitution from the undoped sample until x = 0.15, thereby reaching a maximum zT of 0.11 at 473K. With further increase in the Er amount (x = 0.3 and x = 0.4), the zT deteriorates due to the uncompensated low electrical conductivity values. It is worth mentioning that, the high Seebeck coefficient and low thermal conductivity values for x = 0.3 and x = 0.4 could not compensate for the low electrical conductivity which thus results in low overall TE performance. The optimum zT is obtained for Bi_{1.85}Er_{0.15}Se₃ with a peak value of 0.11 at 473K. This value is approximately 75% higher than that of the pristine (Bi₂Se₃) considered at the same temperature. The improvement seen in the Er-substituted samples is due to the optimized effect of the isovalent substitution on the power factor and the thermal conductivity of the Bi_{2-x}Er_xSe₃. The low thermal conductivities found for x = 0.3 and x = 0.4 could not pay off for the low electrical conductivity, which thus degrades the TE performance of the highly substituted samples.

4. Conclusion

In conclusion, we have successfully synthesized high purity Bi_{2-x}Er_xSe₃ (0, 0.15, 0.3, and 0.4) through a facile single-step solvothermal route, and their TE properties are evaluated. The TE performance of Bi_{2-x}Er_xSe₃ (for x > 0) shows a simultaneous enhancement of Seebeck coefficient and electrical conductivity coupled with a significant decrease in the total thermal conductivity, thus increasing the power factor and zT. The best performance is found for Bi_{1.85}Er_{0.15}Se₃ with PF_{max}, K_{Tmin}, and zT_{max} of 99.4 μWm⁻¹ K⁻², 0.41 Wm⁻¹K⁻¹, and 0.11 at 473K. The improved performance in Bi₂Se₃ with less Er substitution signifies a salient role of rare earth elements in decoupling the transport properties of TE materials. The current study sheds light on the realization of simultaneous enhancement in the Seebeck coefficient with the reduction in thermal conductivity for Er substitution in bismuth selenide

TE materials. We, therefore, show that Er induces simultaneous enhancement in S and σ which is expected to induce changes in the inverted conduction band of $\text{Bi}_{2-x}\text{Er}_x\text{Se}_3$ topological insulators. Our previous theoretical and experimental studies on Ce substitution in Bi_2Se_3 coupled with the current work (Er substitution) demonstrates that rare earth elements substitution in bismuth selenide can be instrumental in achieving simultaneous enhancement in Seebeck coefficient and electrical conductivity which is crucial for high TE performance.

Acknowledgement

We wish to acknowledge grants from the Research Grants Council of Hong Kong Special Administrative Region Project no. T42-103/16N. VK acknowledges Act 211 Government of the Russian Federation, contract No. 02.A03.21.0011.

Reference

1. Bell, L. E. Cooling, heating, generating power, and recovering waste heat with thermoelectric systems. *Science (80-.)*. **321**, 1457–1461 (2008).
2. Disalvo, F. J. Thermoelectric cooling and power generation. *Science (80-.)*. **285**, 703–706 (1999).
3. Poudel, B. *et al.* High-Thermoelectric Performance of Nanostructured Bismuth Antimony Telluride Bulk Alloys. *Science (80-.)*. **320**, 634–638 (2008).
4. Division, M. S. & Berkeley, L. Nanostructuring Expands Thermal Limits. **2**, 40–47 (2007).
5. Devender; Pascal, Gehring; Andrew, Gaul; Alexander, Hoyer; Kristina, Vaklinova; Rutvik, J. Mehta; Marko, Burghard; Theodorian, Borca - Tasciuc; David, J.Singh; Klaus, Kern; Ganpati, R. Harnessing Topological Band Effects in Bismuth Telluride Selenide for Large Enhancements in Thermoelectric Properties through Isovalent Doping. *Adv. Mater.* 6436–

6441 (2016). doi:10.1002/adma.201601256

6. Vaney, J.-B. *et al.* Effect of Isovalent Substitution on the Electronic Structure and Thermoelectric Properties of the Solid Solution α -As₂Te_{3-x}Se_x ($0 \leq x \leq 1.5$). *Inorg. Chem.* **56**, 2248–2257 (2017).
7. Musah, J.-D. *et al.* Simultaneous Enhancement of Thermopower and Electrical Conductivity through Isovalent Substitution of Cerium in Bismuth Selenide Thermoelectric Materials. *ACS Appl. Mater. & Interfaces* **0**, (2019).
8. Sk, R., Shirolkar, M. M., Dhara, B., Kulkarni, S. & Deshpande, A. Enhancing the thermopower and tuning the resistivity in Bi₂Se₃ with Fe-doping. *Chem. Phys. Lett.* **638**, 94–98 (2015).
9. Bindu, P. & Thomas, S. Estimation of lattice strain in ZnO nanoparticles: X-ray peak profile analysis. *J. Theor. Appl. Phys.* **8**, 123–134 (2014).
10. Fang, C. M., Meetsma, A. & Wieggers, G. A. Crystal Structure of Erbium Sesquiselenide, Er₂Se₃. *J. Alloys Compd.* **218**, 224–227 (1995).
11. Özgür, Ü. *et al.* A comprehensive review of ZnO materials and devices. *J. Appl. Phys.* **98**, 1–103 (2005).
12. Rajakarhikeyan, R. K. & Muthukumaran, S. Investigation of microstructure, electrical and photoluminescence behaviour of Ni-doped Zn_{0.96}Mn_{0.04}O nanoparticles: Effect of Ni concentration. *Opt. Mater. (Amst)*. **69**, 382–391 (2017).
13. Sangeetha, R. & Muthukumaran, S. Bandgap tailoring and enhanced visible emission by two-step annealing in Zn_{0.94}Cu_{0.04}Cr_{0.02}O nanocrystals. *J. Mater. Sci. Mater. Electron.* **26**, 9667–9679 (2015).
14. Rusu, V. M. *et al.* Size-Controlled Hydroxyapatite Nanoparticles as Self-Organized Organic-Inorganic Composite Materials. *Biomaterials* **26**, 5414–5426 (2005).
15. Ammar, A. H., Abo Ghazala, M. S., Farag, A. A. M. & Eleskandrany, A. Influence of

- Composition on Structural, Electrical and Optical Characterizations of Bi_{48-x}Sb_xSe₅₂ Ternary Chalcogenide System. *Indian J. Phys.* **87**, 1169–1175 (2013).
16. Bohra, A. K. *et al.* Tellurium-free thermoelectrics: Improved thermoelectric performance of n-type Bi₂Se₃ having multiscale hierarchical architecture. *Energy Convers. Manag.* **145**, 415–424 (2017).
 17. Proctor, K. J., Regan, K. A., Littman, A. & Disalvo, F. J. Thermoelectric properties of the intermediate valent cerium intermetallic Ce₂Ni₃Si₅ doped with Pd, Co, and Cu. *J. Alloys Compd.* **292**, 124–128 (1999).
 18. Zhang, J. *et al.* Raman Spectroscopy of Few-Quintuple Layer Topological Insulator Bi₂Se₃ Nanoplatelets. *Nano Lett.* **11**, 2407–2414 (2011).
 19. Dang, W., Peng, H., Li, H., Wang, P. & Liu, Z. Epitaxial Heterostructures of Ultrathin Topological Insulator Nanoplate and Graphene. *Nano Lett.* **10**, 2870–2876 (2010).
 20. Zhao, S. Y. F. *et al.* Fabrication and Characterization of Topological Insulator Bi₂Se₃ Nanocrystals. *Appl. Phys. Lett.* **98**, 96–99 (2011).
 21. Childres, I., Tian, J., Miotkowski, I. & Chen, Y. AFM and Raman Studies of Topological Insulator Materials Subject to Argon Plasma Etching. *Philos. Mag.* **93**, 681–689 (2013).
 22. Richter, W. & Becker, C. Raman and far-infrared investigation of phonons in the rhombohedral V₂–VI₃ compounds Bi₂Te₃, Bi₂Se₃, Sb₂Te₃ and Bi₂(Te_{1-x}Se_x)₃ (0 < x < 1), (Bi_{1-y}Sb_y)₂Te₃. *Phys. Status Solidi* **84**, 619–628 (2006).
 23. Richter, W., Kohler, H. & Becker, C. R. A Raman and Far-Infrared Investigation of Phonons in the Rhombohedral V₂-VI₃ Compounds. *Phys. Stat. Sol.* **84**, 619, (1977).
 24. Khyzhun, O. Y., Halyan, V. V., Danyliuk, I. V. & Ivashchenko, I. A. Electronic Structure of (Ga₅₅In₄₅)₂S₃₀₀ and (Ga_{54.59}In_{44.66}Er_{0.75})₂S₃₀₀ Single Crystals. *J. Mater. Sci. Mater. Electron.* **27**, 3258–3264 (2016).

25. Ramasamy, P., Chandra, P., Rhee, S. W. & Kim, J. Enhanced Upconversion Luminescence in NaGdF₄: Yb, Er Nanocrystals by Fe³⁺ Doping and their Application in Bioimaging. *Nanoscale* **5**, 8711–8717 (2013).
26. Liu, S., Peng, N., Zhou, C., Bai, Y. & Tang, S. Fabrication of Bi₂Te_{3-x}Se_x nanowires with tunable chemical compositions and enhanced thermoelectric properties. *Nanotechnology* **28**, (2017).
27. Wang, Z., Qiu, W., Yang, Y. & Liu, C. T. Atomic-size and lattice-distortion effects in newly developed high-entropy alloys with multiple principal elements. *Intermetallics* **64**, 63–69 (2015).
28. Eshelby, J. . *The Continuum Theory of Lattice Defects. Solid State Physics*. (Academic Press, 1956).
29. Snyder, G. J. & Toberer, E. S. Complex thermoelectric materials. *Nat. Mater.* **7**, 105–114 (2008).
30. Wu, F., Song, H., Jia, J. & Hu, X. Effects of Ce, Y, and Sm Doping on the Thermoelectric Properties of Bi₂Te₃ Alloy. *Prog. Nat. Sci. Mater. Int.* **23**, 408–412 (2013).
31. Tritt, T. M. & Subramanian, M. a. Thermoelectric Materials, Phenomena, and Applications : A Bird's Eye View. *MRS Bull.* **31**, 188–198 (2006).
32. Mishra, S. K., Satpathy, S. & Jepsen, O. Electronic Structure and Thermoelectric Properties of Bismuth Telluride and Bismuth Selenide. *J. Phys. Condens. Matter* **9**, 461–470 (1997).
33. Frey, H. Electronic structure and thermoelectric properties of bismuth telluride and bismuth selenide Electronic structure and thermoelectric properties of bismuth telluride and bismuth selenide. 375, (2015).
34. Shuai, J. *et al.* Tuning the carrier scattering mechanism to improve the thermoelectric properties effectively. *Energy Environ. Sci.* **10**, 799–807 (2017).

35. Wu, H. *et al.* Strong Enhancement of Phonon Scattering through Nanoscale Grains in Lead Sulfide Thermoelectrics. *NPG Asia Mater.* **6**, (2014).
36. Rowe, D. M. & Shukla, V. S. The Effect of Phonon-Grain Boundary Scattering on the Lattice Thermal Conductivity and Thermoelectric Conversion Efficiency of Heavily Doped Fine-Grained, Hot-Pressed Silicon Germanium Alloy. *J. Appl. Phys.* **52**, 7421–7426 (1981).
37. Kishimoto, K. & Koyanagi, T. Preparation of Sintered Degenerate n-Type PbTe with a Small Grain Size and its Thermoelectric Properties. *J. Appl. Phys.* **92**, 2544–2549 (2002).
38. Shi, H., Parker, D., Du, M. H. & Singh, D. J. Connecting thermoelectric performance and topological-insulator behaviour: Bi₂Te₃ and Bi₂Te₂Se from first principles. *Phys. Rev. Appl.* **3**, 1–10 (2015).

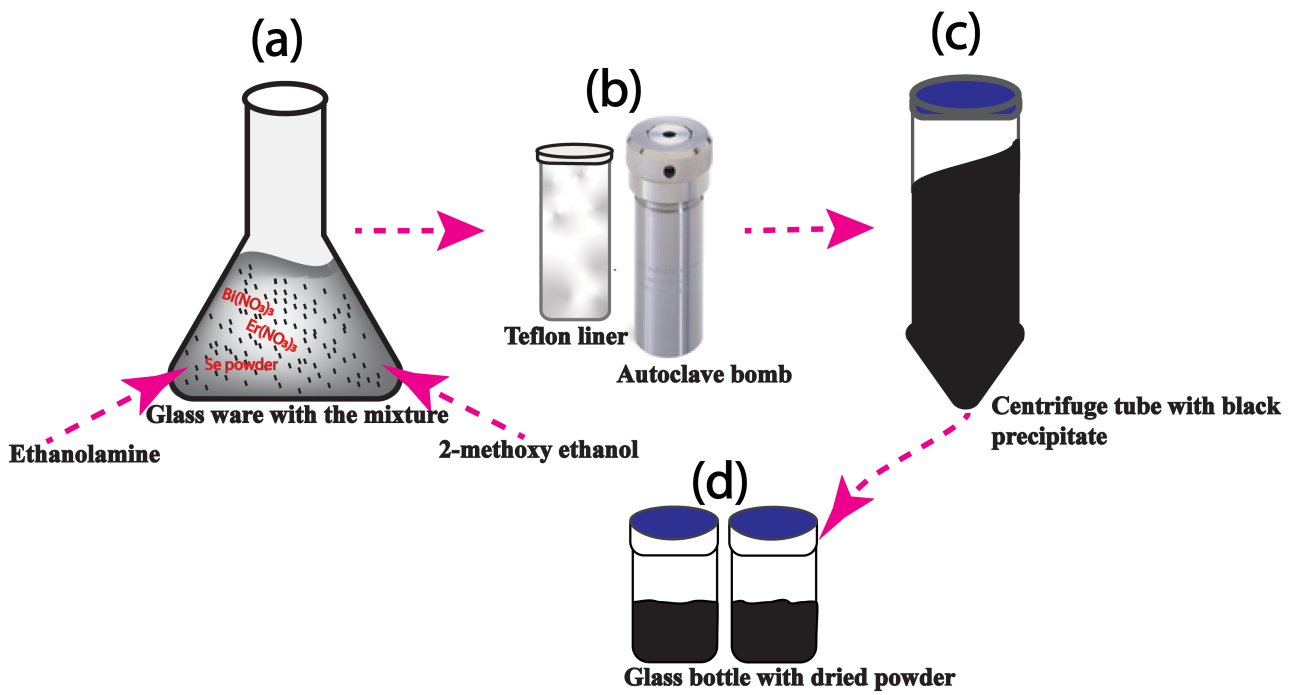


Figure 1. The synthesis procedure of the $\text{Bi}_{2-x}\text{Er}_x\text{Se}_3$ samples (a) The precursor powders are mixed with a required volume ratio of ethanolamine and 2-methoxy ethanol which is then kept under constant stirring for homogeneity. (b) the black mixture is then transferred into an autoclave and kept in an oven for a day. (c) the black precipitate is collected and washed several times with water (d) the final $\text{Bi}_{2-x}\text{Er}_x\text{Se}_3$ black powder after drying at 343K for half a day.

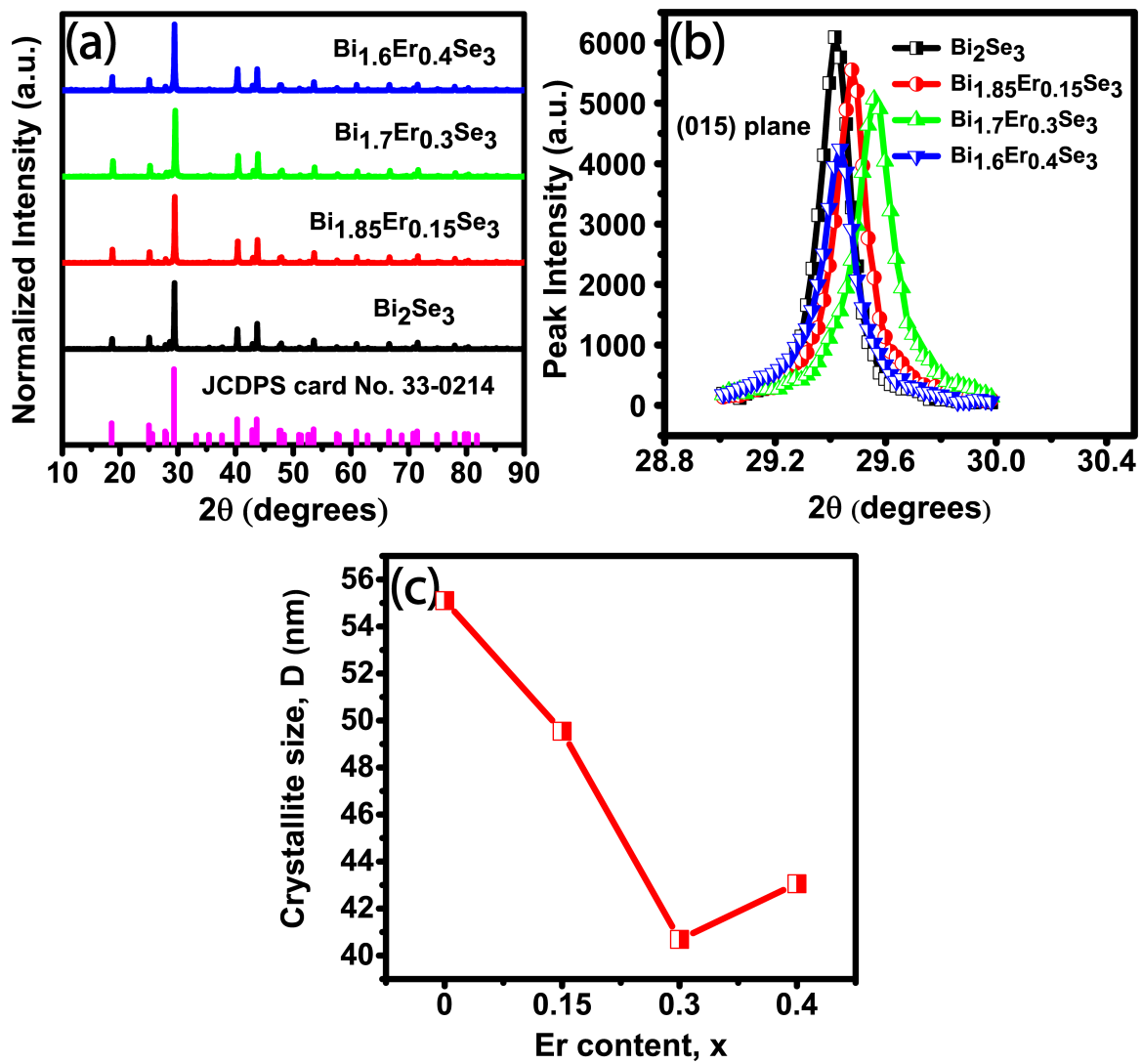


Figure 2. (a) The normalized XRD pattern of as-prepared $\text{Bi}_{2-x}\text{Er}_x\text{Se}_3$ samples (b) peak intensity of the (015) plane showing a shift in the 2θ (c) the variation of the crystallite size dependence on the Er content.

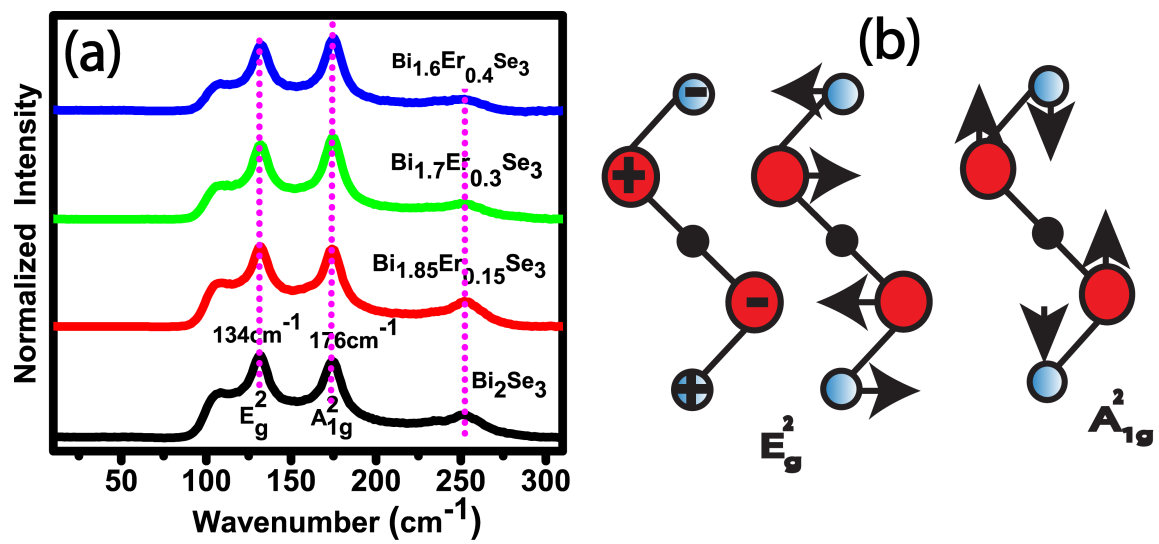


Figure 3. (a) The Raman spectra of the $\text{Bi}_{2-x}\text{Er}_x\text{Se}_3$ samples and (b) the Raman active vibrational mode of the rhombohedral $\text{V}_2\text{-VI}_3$ compounds,

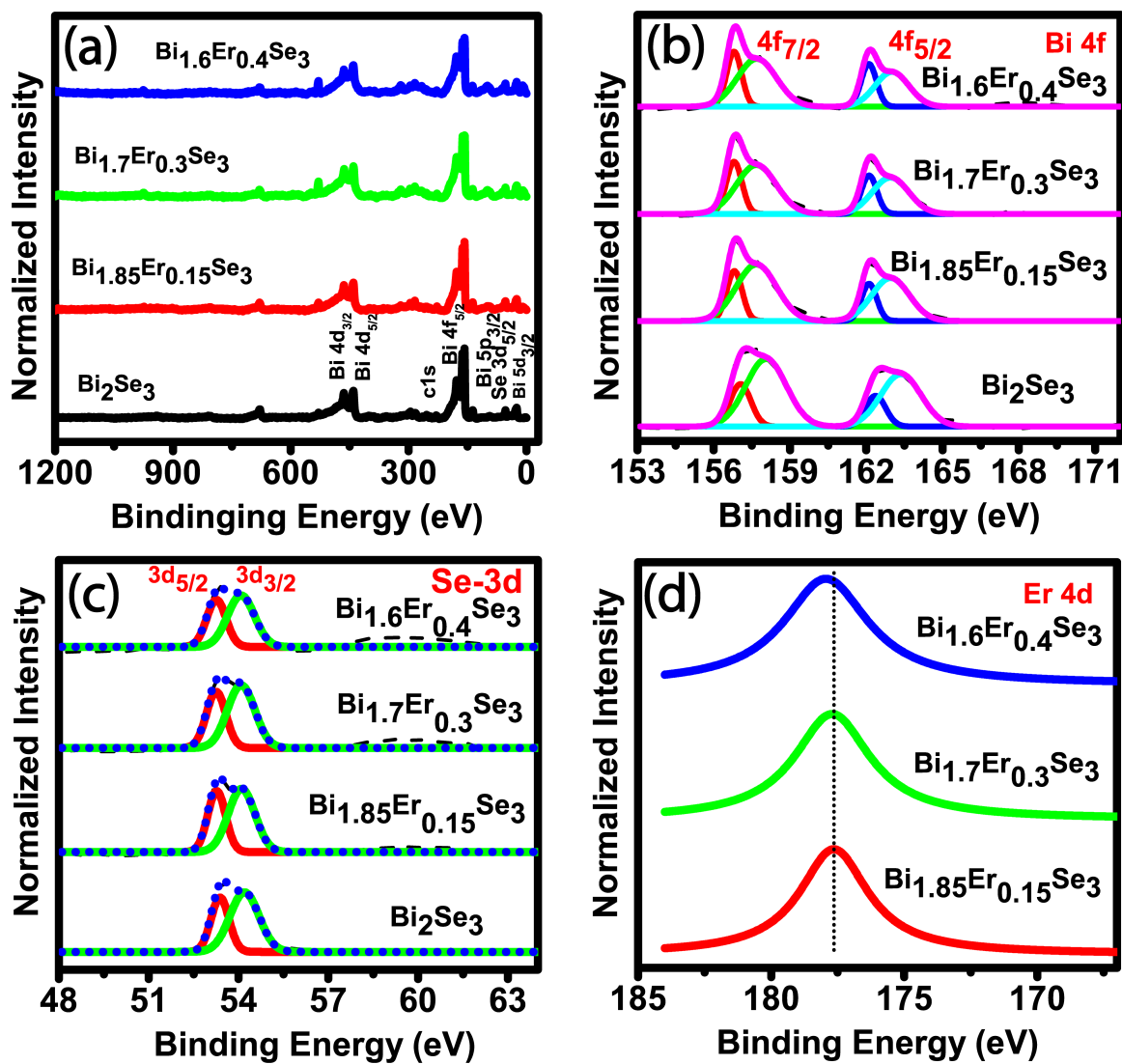


Figure 4. The XPS spectra of the $\text{Bi}_{2-x}\text{Er}_x\text{Se}_3$ samples for (a) 100 nm full range survey scan (b) high-resolution spectra of the Bi 4f core-level (c) high-resolution scan of Se 3d spectra and (d) high-resolution scan of Er 4d spectra.

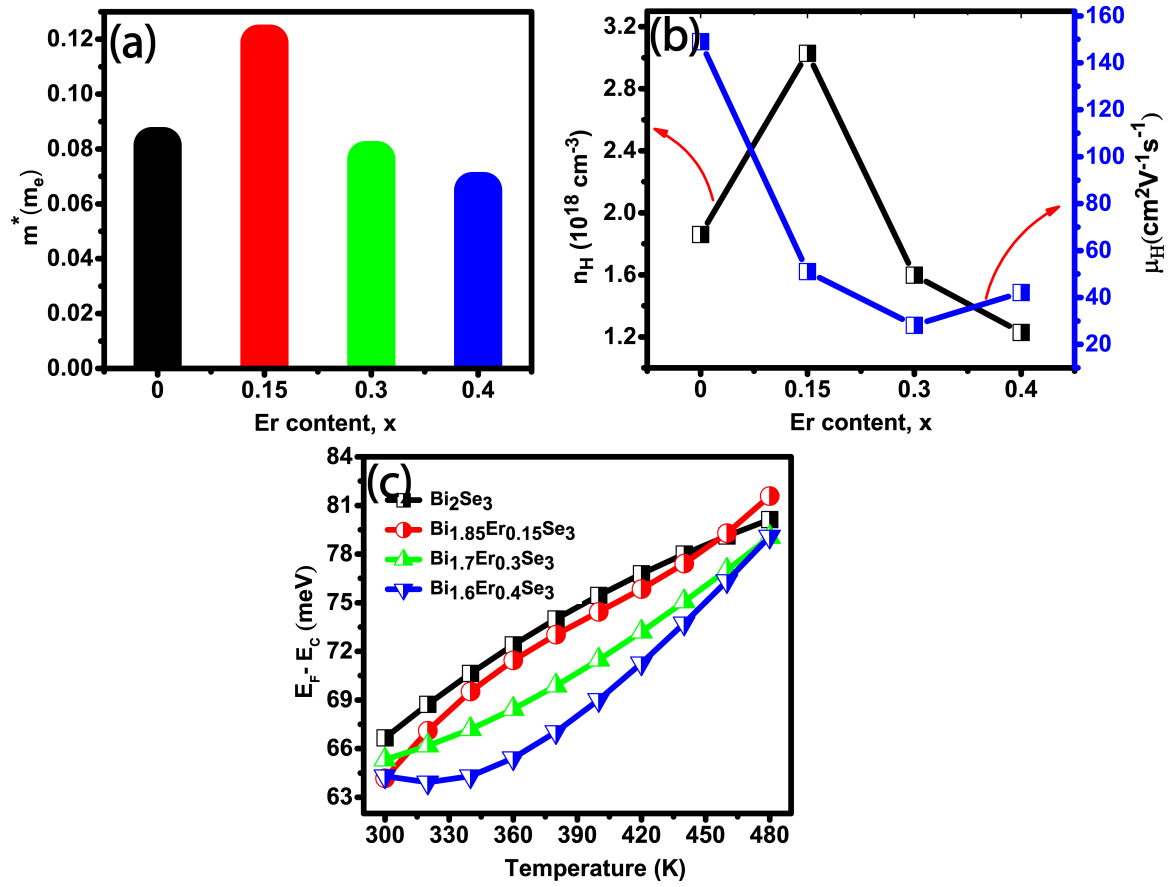


Figure 5. (a) The dependence of effective carrier mass on the Er content, (b) Room temperature Hall data on the Er content, and (c) temperature dependence of the Fermi energy.

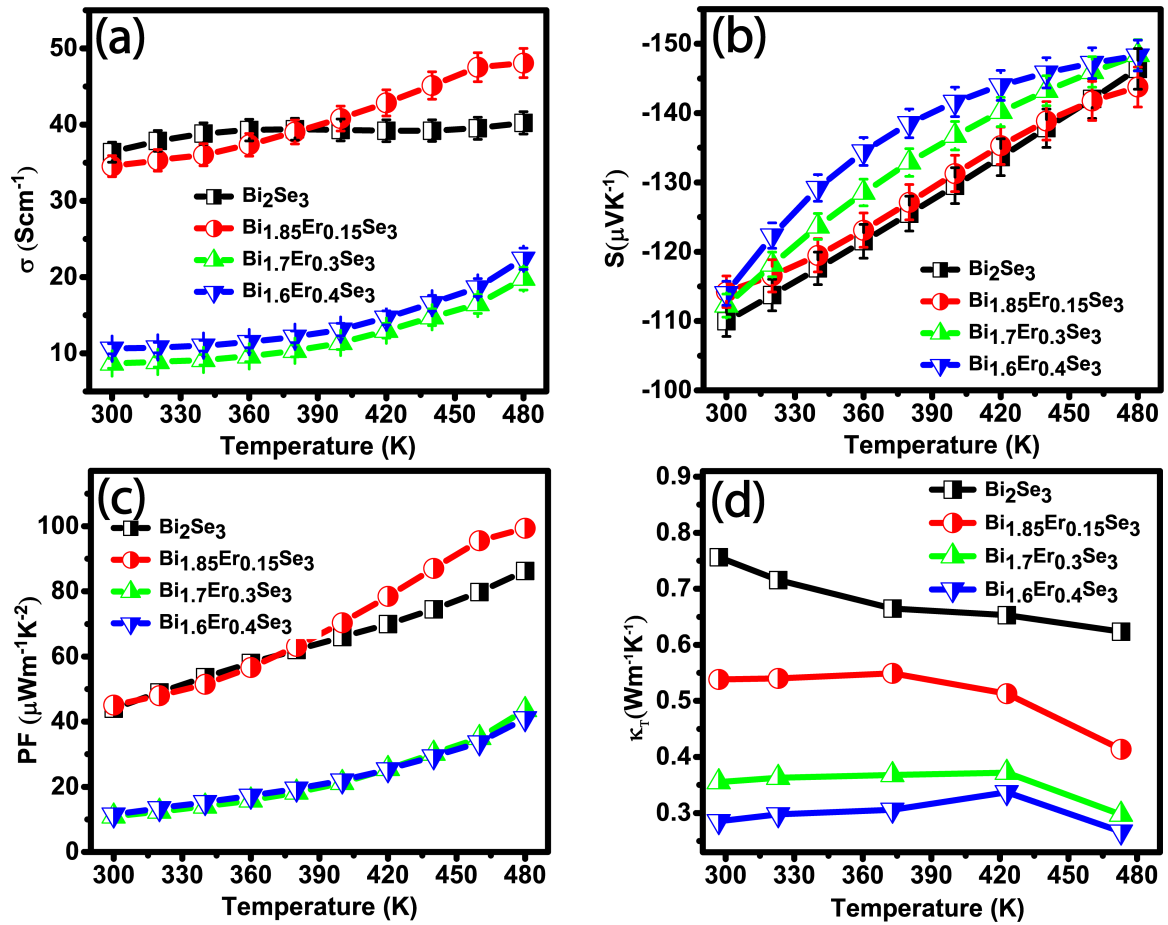


Figure 6. Temperature-dependent (a) electrical properties, (b) Seebeck coefficient, (c) power factor, and (d) total thermal conductivity of the Bi_{2-x}Er_xSe₃ thermoelectric material.

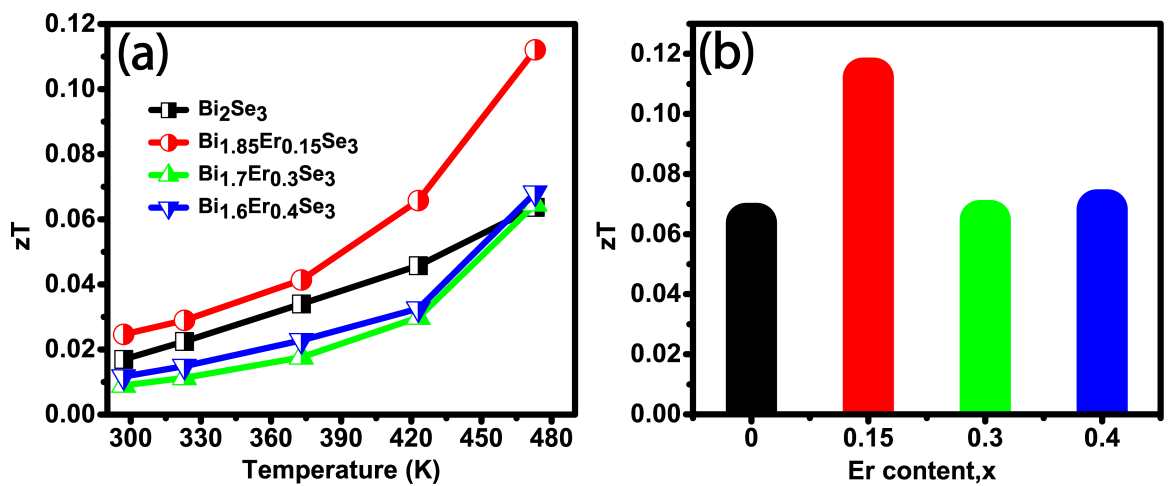


Figure 7. The dependence of the thermoelectric figure of merit as a function of (a) temperature (b) Er content at 473K.